coatings

MDPI

*Article*

# Electrochemical Properties of $LiNi_{0.6}Co_{0.2}Mn_{0.2}O_2$ Cathode Materials Prepared with Different Ammonia Content

**Chen Xu, Siqi Guan, Lixiang Li, Chengguo Sun, Baigang An and Xin Geng ***

Key Laboratory of Energy Materials and Electrochemistry Research Liaoning Province, University of Science and Technology Liaoning, Anshan 114051, China; chen_x0326@163.com (C.X.); siqi_g07@163.com (S.G.); lxli2005@126.com (L.L.); sunyangguo@163.com (C.S.); baigang73@126.com (B.A.)
* Correspondence: gengxin60@163.com

**Abstract:** The content of ammonia coordination agent in initial aqueous solution is one of important factors which greatly influences the morphologies and electrochemical performances of layered $LiNi_6Mn_2Co_2O_2$ (NCM622). The spherical morphologies, contributing to higher specific capacity of NCM622, ascribe to the same precipitation rate of transition metal ions ($Ni^{2+}$, $Co^{2+}$, $Mn^{2+}$) during co-precipitation. Hence, the effects of different amounts of ammonia in initial solution on the hydroxide equilibrium constant and properties of NCM622 were discussed. With the ammonia content of 70 mL, the spherical morphology with more perfect layered structure and higher discharge capacity are obtained. The necessity of ammonia content in initial solution are also demonstrated from electrochemical performances of NCM622, such as the initial discharge capacity of 199.8 mAh $g^{-1}$ at 0.1 C, the specific capacity of 150.0 mAh $g^{-1}$ after 100th cycles, and the capacity retention rate of 89.6% at 3 C. If other metal ions are anticipated to be chemically doped with NCM622, the hydroxide equilibrium constant and precipitation rate need to be considered.

**Keywords:** lithium ion batteries; hydroxide co-precipitation method; NCM ternary precursor; electrochemical performance



**Citation:** Xu, C.; Guan, S.; Li, L.; Sun, C.; An, B.; Geng, X. Electrochemical Properties of $LiNi_{0.6}Co_{0.2}Mn_{0.2}O_2$ Cathode Materials Prepared with Different Ammonia Content. *Coatings* **2021**, *11*, 932. https://doi.org/10.3390/coatings11080932

Academic Editor: Octavian Buiu

Received: 29 June 2021
Accepted: 28 July 2021
Published: 4 August 2021



## 1. Introduction

In recent years, with the increasing energy crisis and environmental pollution [1], the demand for new energy has been increasing, and then the development of a typical new energy material became critical. The different types of Batteries has been developing rapidly, among which lithium-ion battery has been paid much attention [2,3]. Because of their high energy densities and long cycle span, lithium-ion batteries (LIB) have been wide spread applied in personal electronic devices, electric vehicles (EV), and energy-storage systems [4,5]. The specific capacity of the cathode material in the lithium battery is far less than their theoretical capacity [6,7]. Therefore, it is necessary to develop lithium ion cathode materials with larger capacity, better stability and lower cost [8]. At present, the commercial cathode materials mainly include $LiMnO_2$ [9–11], $LiCoO_2$ [12], $LiFePO_4$ [13,14], $LiNiO_2$ [15,16] and layered $LiNiMnCoO_2$ (NCM) [17–19]. NCM has attracted wide attention due to its high electrochemical performances, long cycle life, high specific power and specific energy.

Now there are ways to prepare precursors of NCM by co-precipitation method, such as hydrothermal method [20,21], spray pyrolysis method [22,23], sol-gel method and high temperature solid state reaction method [24], et al. With the advantages of low synthesis temperature, facile morphology control, simple process, and convenient industrialization, the co-precipitation method is chosen to prepare the precursors of NCM. The ammonia content in base-solution has an important effect on the physical characteristic of precursor by co-precipitation method.

As shown in Table 1, the $K_{sp,\,M(OH)n}$ (precipitation equilibrium constant) of $Ni(OH)_2$, $Co(OH)_2$ is four orders of magnitude higher than that of $Mn(OH)_2$. If $Ni^{2+}$, $Co^{2+}$ and

$Mn^{2+}$ are directly precipitated with NaOH precipitant, manganese hydroxide is precipitated first, which will bring about $Mn(OH)_2$ partly separated with $Ni(OH)_2$, $Co(OH)_2$. When they are calcined with lithium hydroxide at high temperature, the mixture including $LiNiO_2$, $LiCoO_2$, $LiMn_2O_4$ or $LiNiCoMnO_2$, etc, instead of pure ternary lithium ion materials, are prepared. Because the particles of the mixture are both uncontrolled and easily fractured during the charge-discharge, the whole electrochemical performances will also be restrained. As for the coordination effect of ammonia with $Ni^{2+}$, $Co^{2+}$, and $Mn^{2+}$, Yabin Shen et al. [25]. calculated the precipitation equilibrium constant of $Ni^{2+}$, $Co^{2+}$ and $Mn^{2+}$ with $OH^-$, respectively (shown in Table 1). Owing to mass $NH_4{}^-$ existing in initial solution, $Ni^{2+}$, $Co^{2+}$ and $Mn^{2+}$ react with $NH_4{}^-$ prior to with $OH^-$, which will depress the precipitation rate of $Mn(OH)_2$ to the level of $Ni(OH)_2$, $Co(OH)_2$. The uniform and slow precipitation of $Ni^{2+}$, $Co^{2+}$ and $Mn^{2+}$ in the co-precipitation process is favourable to develop the uniform accumulation and larger size particles of the precursors. Although ammonia contents in base-solution play an important role the physical characteristic of precursor and NCM622, few research were made. Therefore, it is necessary to explicate the couple relation different ammonia concentration, the morphology of the precursors and electrochemical properties of NCM622.

**Table 1.** $Ni^{2+}$, $Co^{2+}$ and $Mn^{2+}$ before and after the addition ammonia of $K_M$.

| Name of Metal Ion | $K_M$ (Before Add Ammonia) | $D_M$ | $K_M$ (After Add Ammonia) |
|---|---|---|---|
| $Ni^{2+}$ | $10^{14.7}$ | $10^{-5.59}$ | $10^{9.11}$ |
| $Co^{2+}$ | $10^{14.8}$ | $10^{-5.46}$ | $10^{9.34}$ |
| $Mn^{2+}$ | $10^{10.74}$ | $10^{-1.51}$ | $10^{9.23}$ |

In this work, we observed the couple connection among the amounts of ammonia in base-solution, the morphology of the precursors and special capacity of NCM622. The precursors of NCM622 were prepared by a hydroxide co-precipitation with the 5 M ammonia and 4 M NaOH added into base-solution, accompanying dissolution of smaller particles and redeposition on larger particles in the solution. The morphology of the precursor was controlled by changing the amounts of ammonia in base-solution to explore the physical and electrochemical effects of different ammonia amounts on the NCM622. Considering ammonia added into deionized water before co-precipitation reaction, large fluctuation of pH in reactor at the beginning of the reaction will be avoided. As a result, sphericity and compactness of secondary particles of precursors will also controlled by the dissolution and reprecipitation of primary particles of precursors. Consequently, high specific capacity and good stability of NCM622 can be anticipated.

## 2. Materials and Methods

### *2.1. Experimental Materials*

Manganese sulfate monohydrate($MnSO_4 \cdot H_2O$), AR, Aladdin Reagents (Shanghai) Co., Ltd., Shanghai, China. Nickel sulfate hexahydrate($NiSO_4 \cdot 6H_2O$), AR, Aladdin Reagents (Shanghai) Co., Ltd.; Cobalt sulfate heptahydrate($CoSO_4 \cdot 7H_2O$), AR, Aladdin Reagents (Shanghai) Co., Ltd.; Ammonia solution($H_5NO$), 25%–28%, Sinopharm Chemical Reagent Co. Ltd., Shanghai, China; Sodium hydroxide(NaOH), AR, Sinopharm Chemical Reagent Co. Ltd.; Lithium hydroxide monohydrate($LiOH \cdot H_2O$), AR, Aladdin Reagents (Shanghai) Co., Ltd.; Akema HSV900 PVDF binder for Li-ion Battery Electrodes; 1-Methyl-2-pyrrolidinone (NMP), 99.9%, Aladdin Reagents (Shanghai) Co., Ltd.; TIMCAL Graphite & Carbon Super P Conductive Black; aluminum foil, 20 μm; battery case, CR2032; Plate, φ16 * 1.0 mm; steel disc, φ16 * 1.0 mm. 1 M $LiPF_6$ in a 1:1:1 mixture of EC:DMC:EMC; HF-Kejing OTF-1200X tube furnace, vacuum drying oven, Hefei Department of crystal material Technology Co., Ltd, Hefei, China; MERAUN Ar-filled glovebox, Meraun Inert Gas Systems (Shanghai) Co., Ltd, Shanghai, China; Kejing benchtop experimental coater, Hefei Department of crystal material Technology Co., Ltd, Hefei, China.

### 2.2. Materials Synthesis

Typically, the solution of $NiSO_4 \cdot 6H_2O$, $CoSO_4 \cdot 7H_2O$, and $MnSO_4 \cdot H_2O$ (2 mol $L^{-1}$, cationic ratio of Ni:Co:Mn = 6:2:2, named NCM622) was continuously fed into a stirred tank reactor with the different content of ammonia (ammonia solution of 40 mL, 50 mL, 60 mL and 70 mL in deionized water of 1 L, respectively, they are named as NCM622 (AC: 40 mL), NCM622 (AC: 50 mL), NCM622 (AC: 60 mL), and NCM622 (AC: 70 mL)) in base-solution at a flow rate of 1.2 mL $min^{-1}$ under $N_2$ atmosphere. Simultaneously, appropriate amount of NaOH solution (4 mol $L^{-1}$, used as the precipitation agent and the adjustment of pH value), $NH_4OH$ solution (5 mol $L^{-1}$, used as chelator) were added into the reactor separately. The pH value of 11, temperature of 55 °C and stirring speed of 800 rpm were carefully controlled by the flow rate of the dropwise. Then, the precursor powder was washed, filtered and dryed in a vacuum oven for 12 h. The precursor of $Ni_{0.6}Co_{0.2}Mn_{0.2}(OH)_2$ was mixed with $LiOH \cdot H_2O$ at a molar ratio of 1:1.05 through ball milling. And Lithium precursors were heated at 480 °C for 5 h in oxygen atmosphere. The obtained material was milled again and then calcined at 850 °C for 12 h under an oxygen atmosphere.

### 2.3. Materials Characterizations

To analyze the structure of the material, XRD (D8 Advance Germany Bruker) with Cu−K$\alpha$ radiation was utilized and MDI Jade 6 software was used to conduct Rietveld refinement. The particle morphologies were observed by scanning electron microscopy (SEM, FEI Apreo), Thermo Fisher Scientific, Waltham, MA, USA.

### 2.4. Electrochemical Measurements

The electrode slurry was manufactured by dispersing 80 wt % active materials, 10 wt % Super P, and 10 wt % PVDF in NMP solution thoroughly. The obtained slurry was coated evenly onto Al foil and dried at 80 °C for 12 h in a vacuum oven. The CR2032 coin cells were assembled in an Ar-filled glovebox, utilizing a Cellgard 2300 separator, Li metal as the anode, and 1 M LiPF6 in a 1:1:1 mixture of EC:DMC:EMC as electrolyte. The cells were tested with a voltage window between 2.5 and 4.5 V (1 C = 200 mA $g^{-1}$) vs. $Li/Li^+$ at 25 °C by LAND. test system. Electrochemical impedance spectroscopy (EIS) was conducted at a GAMRY Reference 3000 chemical workstation from 100 kHz to 10 mHz. Cyclic voltammetry (CV) was conducted on a CHI760D chemical workstation at voltage range of 2.8–4.5 V and scan rate of 0.1 mV $s^{-1}$.

## 3. Results

The morphology changes of the precursors resulted from the mechanism of Oswald ripening mechanism [26]. $M^{2+}$ and $OH^-$ collide each other through thermal motion to form a smaller crystal nucleus. Due to far less surface energy of larger particles than that of smaller particles, Smaller grains in the ammonia and sodium hydroxide aqueous solution will be dissolved for the energy balance of whole system. While all hydroxides are in supersaturation state, they will be redeposited on the larger grains by the secondary nucleation process. With the progress of the dissolution and re-deposition step by step, the grains of all hydroxides will are enlarged simultaneously and accumulated into bigger spherical grains for the sake of minimum energy systems. If the re-deposition rate of ternary precursor is too fast during crystallization, $\alpha$-type $Ni(OH)_2$ and $Mn(OH)_2$ with poor crystallinity will be formed. High concentration aqueous ammonia in the ammonia and sodium hydroxide aqueous solution will retard the re-deposition rate. Based on the precipitation equilibrium constant of nickel hydroxide, cobalt hydroxide and manganese hydroxide and metal ions and ammonia coordinate stability constants, the relationships of ammonia amounts to the reaction degree of $Ni^{2+}$, $Co^{2+}$ and $Mn^{2+}$ with $OH^-$ were calculated (shown in Figure 1). With the increase of ammonia amounts, the more residual amount of $Ni^{2+}$, $Co^{2+}$ and $Mn^{2+}$ remained. However, when the amounts are lower, due to the poor coordination effect between ammonia and $Ni^{2+}$, $Co^{2+}$ and $Mn^{2+}$, $Ni(OH)_2$, $Co(OH)_2$ were

preferentially precipitated out from the solution exclusive of $Mn(OH)_2$. Therefore, the ammonia concentration between 0.5 and 1 mol $L^{-1}$, which exactly corresponded to the ammonia amounts of 40, 50, 60 and 70 mL, was explorated.

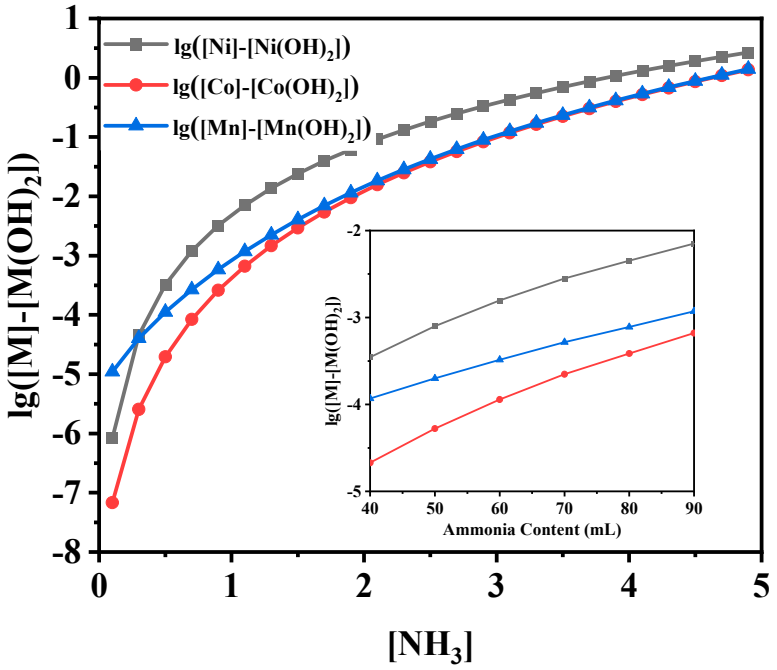


**Figure 1.** Relationship between total concentrations of metal ions and ammonia concentrations.

Given the fact that electrochemical performance of cathode materials is largely depends on its structural characteristics, XRD were used to deduce accurate lattice constants of samples by taking advantage of the intrinsic high resolution of X-ray radiation. Therefore, the structure properties of samples from different ammonia content were analyzed through XRD patterns, as shown in Figure 2a and the deduced structural parameters are given in Table 2. All samples presented similar sharp diffraction lines strongly associated with the hexagonal R3m space group of α-$NaFeO_2$ [27]. The position of each diffraction peak strictly corresponded to the standard map of $LiNiO_2$ (PDF#09-0063). It is well known that the oxygen sub-lattice in the α-$NaFeO_2$ type structure forms a close-packed face centered cubic (fcc) lattice with a distortion in the c direction, which results in the obvious splitting of the peaks (006)/(102) and (108)/(110) in the XRD pattern. Explicit splitting of the (006)/(102) and (108)/(110) peaks demonstrated the highly ordered layer structure of all samples [28,29]. The Peak shapes were sharp, clear, and high intensity of diffraction peak, without impurity peak, indicating that the samples revealed a high crystallinity and regularly crystal structure. With the increase of ammonia content, lattice parameter decreased linearly which meaned reduction of M-O distance. The peak strength ratio of I(003) to I(104) indicated the degree of Li-Ni exchange [30]. The higher the ratio was, the lower the degree of Li-Ni exchange was. With the increase of ammonia content, the rate of I(003) to I(104) increased linearly given in Table 2, indicating that the exchange of lithium and nickel in the material was low.

**Table 2.** XRD parameters of NCM622 different ammonia content.

| NCM622 | a(Å) | c(Å) | c/a | I(003)/I(104) |
|---|---|---|---|---|
| AC: 40 mL | 3.10 | 12.80 | 4.13 | 1.34 |
| AC: 50 mL | 2.87 | 14.23 | 4.95 | 1.37 |
| AC: 60 mL | 2.87 | 14.23 | 4.89 | 1.41 |
| AC: 70 mL | 2.86 | 14.22 | 4.96 | 1.45 |

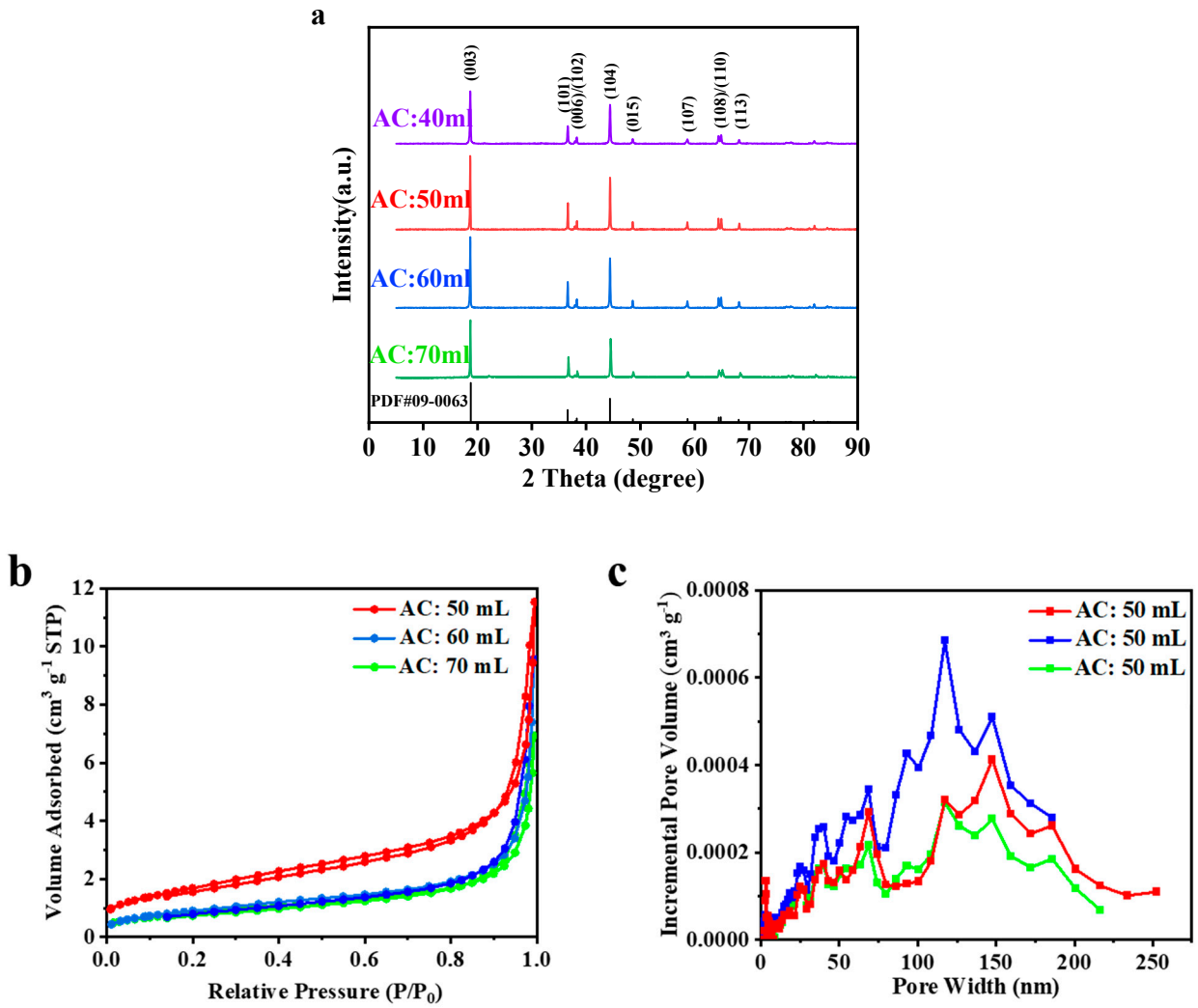


**Figure 2.** (**a**) XRD patterns of NCM622 different from ammonia content. (**b**,**c**) Nitrogen adsorption isotherm and Pore size distribution of NCM622 different ammonia content.

The structural characteristics of NCM622 had also impact on its $N_2$ adsorption features and pore size distribution (shown in Figure 2b,c). With the increase of ammonia content in base-solution, the hysteresis loop in the nitrogen adsorption isotherm gradually disappeared. The results showed that the accumulated mesoporous and macropores in ternary materials gradually disappeared, ascribable to the more compact secondary pelleting [31]. The pore characteristics of different ammonia content samples as shown in Table 3. When the ammonia content is 70 mL, its specific surface area is the smallest, and the pore distribution was basically dominated by macropores, resulting from the accumulation among materials. With the decrease of ammonia content, the specific surface area of ternary materials gradually rised. The larger the specific surface area was, the looser the material was, which was also consistent with the conclusion in the SEM (shown in Figure 3). When the ammonia content was 60 mL, the specific surface area decreased, but the pore volume increased, that is, in the middle state of secondary pellet formation, resulting in the increase of accumulated macropores.

**Table 3.** Pore characteristics of NCM622 different ammonia content.

| Samples | SBET/$m^2$ $g^{-1}$ | Vtotal/$m^3$ $g^{-1}$ | Pore Diameter/nm |
|---|---|---|---|
| AC: 50 mL | 6.2 | 0.0073 | 11.4 |
| AC: 60 mL | 3.4 | 0.0095 | 17.7 |
| AC: 70 mL | 3.1 | 0.0058 | 13.9 |

As illustrated in Figure 3a–d, the secondary particles of the precursors exhibited quasi-spheres with diameter of 5–8 μm, which were accumulated by the needles, sheets, or short sticks of the primary particles. With the increase of ammonia content, on the one hand, the primary particles of the precursor gradually transited from irregular particles to needle and sheet morphologies, which origined from the dissolution and recrystallization of the primary particles. On the other hand, the primary particles were gradually cumulated into the spherical secondary particles by electrostatic attraction. When the ammonia content was 60 mL, the sphericity of the precursor was better. When the ammonia content was 70 mL, the structure of the precursor was more compact and the lamellar structure became more obvious. After the precursors were calcined at 850 °C, the structure of NCM622 became more compact, especially for the ammonia content of 60 mL and 70 mL as shown in Figure 3e–h. When the ammonia contents in the base-solution were 40 mL and 50 mL, the secondary particles of NCM622 became loose and irregular. Based on the precipitation equilibrium and Oswald ripening mechanism, lower ammonia amounts give rise to poor coordination effect, that is, lower ammonia amount was not enough to complete coordination with all metal ions. As a result, reaction rate of free $Ni^{2+}$, $Co^{2+}$, $Mn^{2+}$ and their ammonia complex ions with sodium hydroxide were significant difference and free $Ni^{2+}$, $Co^{2+}$, $Mn^{2+}$ were predominantly. The grain sizes of the precursors were close to nanoscales and the precursors aging was inhibited. The ternary materials sizes were also limited within nanoscales. More importantly, α-type $Ni(OH)_2$ and $Co(OH)_2$ with poor crystallinity and loose structure were also generated together. The results explored that the ammonia contents had strongly impact on the structure of the secondary particles of the precursors and NCM622. As a result, the increase of ammonia content will improve the tightness of NCM622.

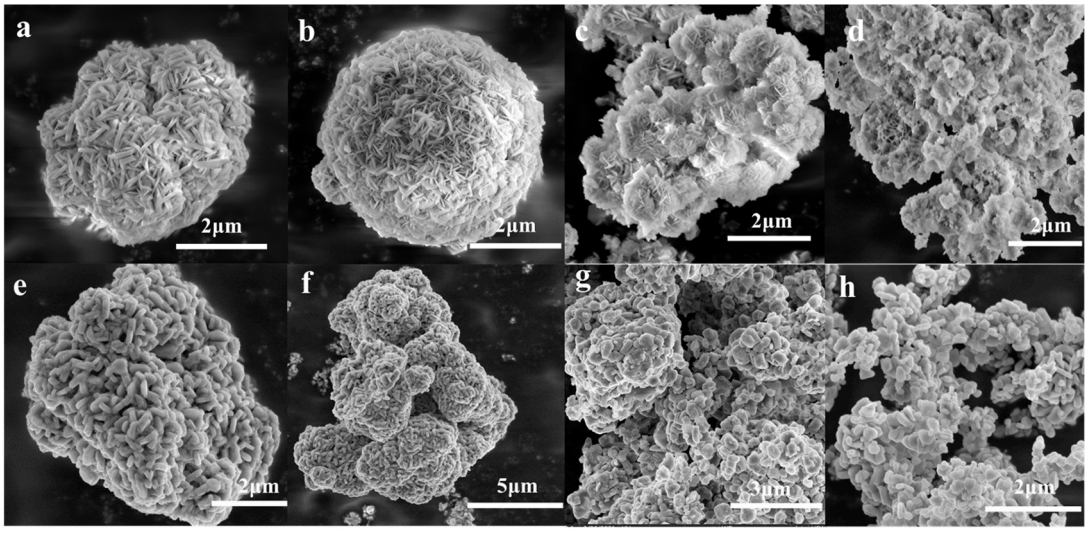


**Figure 3.** SEM images of precursor different ammonia content (**a**) AC: 70 mL. (**b**) AC: 60 mL. (**c**) AC: 50 mL. (**d**) AC: 40 mL. SEM images of NCM622 different ammonia content (**e**) AC: 70 mL. (**f**) AC: 60 mL. (**g**) AC: 50 mL. (**h**) AC: 40 mL.

Figure 4a showed the initial galvanostatic charge-discharge curves of NCM622 from different ammonia contents (AC) between 2.5 and 4.5 V at 0.1 C (20 mA $g^{-1}$) at 25 °C in 2032 coin-type half-cells. The increase of ammonia amount was helpful for the raise

of the charge voltage plateaus and first discharge capacity. As shown in Table 4, the NCM622 (AC: 70 mL) delivered the highest initial discharge capacity of 199.8 mAh $g^{-1}$. In comparison, the NCM622 (AC: 60 mL) cathode exhibited a slightly reduced capacity of 200.0 mAh $g^{-1}$. while the NCM622 (AC: 50 mL) and NCM622 (AC: 40 mL) cathode produces sequentially faded capacity of 186.1 mAh $g^{-1}$ and 184.4 mAh $g^{-1}$. Especially for NCM622 (AC: 40 mL), excessive discharge causes the collapse of lithium ion layer so that the permanent damage of material structure can be restored. With the increase of ammonia content, the structure became more compact, the homogeneous SEI film on the outside surface of NCMs was formed. Consequently, the consumption of electrolyte was less, and the first turn of coulombic efficiency was higher. The total ammonia content of 70 mL was the optimal condition for material synthesis.

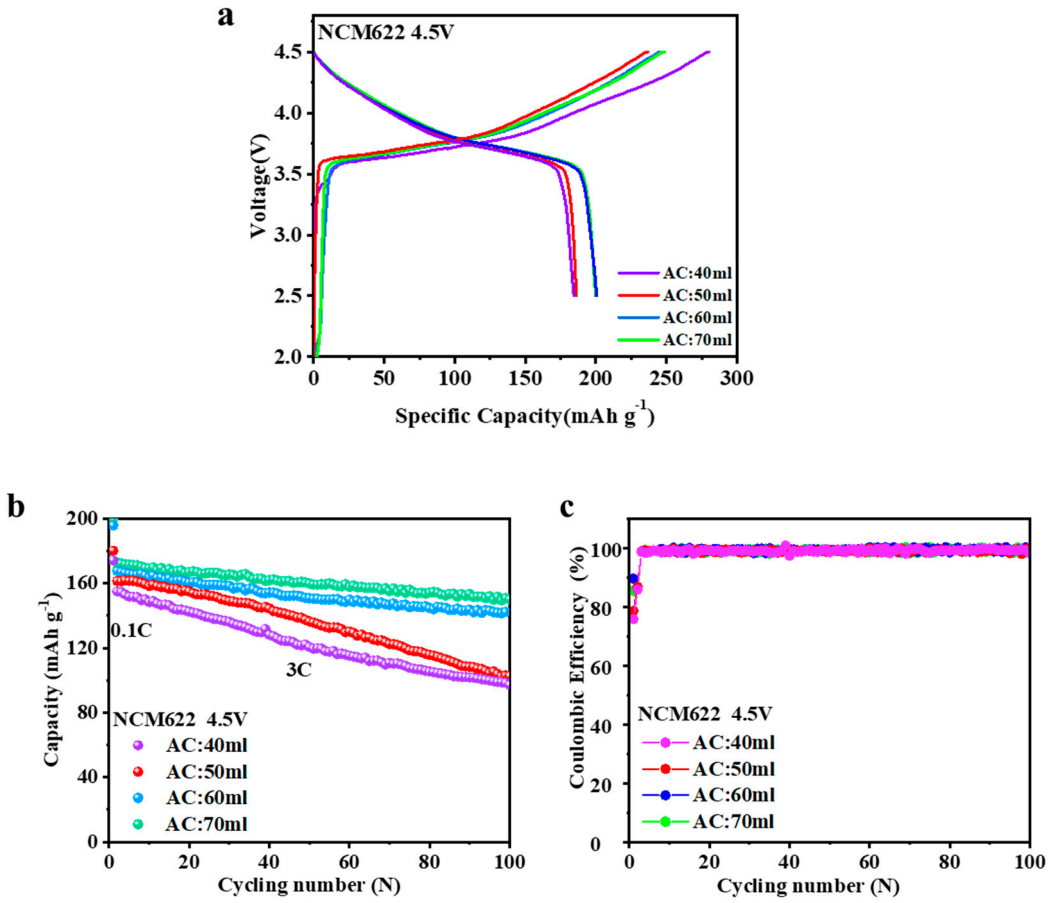


**Figure 4.** (**a**) Initial charge-discharge curves of NCM622 different ammonia content between 2.5 and 4.5 V at 0.1 C. Cycling stability of (**b**) discharge capacities and (**c**) coulombic efficiencies at NCM622 different ammonia content tested with voltage ranges of 2.5−4.5 V at 3 C.

**Table 4.** Initial discharge parameters of NCM622 different ammonia content.

| NCM622 | Discharge Capacity (mAh $g^{-1}$) | Coulombic Efficiency |
|---|---|---|
| AC: 40 mL | 184.4 | 65.8% |
| AC: 50 mL | 186.1 | 78.6% |
| AC: 60 mL | 200.0 | 81.4% |
| AC: 70 mL | 199.8 | 81.0% |

For the purpose of exploring the effect of different ammonia content on the cycling performances, charge−discharge tests were conducted 100 cycles at 3 C between 2.5 and 4.5 V (as show in Figure 4b,c). As shown in Table 5, the NCM622 (AC: 70 mL) maintains

a reversible capacity of 150.0 mAh $g^{-1}$ after 100 cycles with 0.102% decay per cycle. The NCM622 (AC: 60 mL) maintains a reversible capacity of 142.3 mAh $g^{-1}$ after 100 cycles with 0.118% decay per cycle. However, NCM622 (AC: 50 mL) and NCM622 (AC: 40 mL) presented lightly worse cycling retention rates of 63.6% and 62.7%. The decay of capacity retention rate originated from their structure properties, namely, if NCMs were relatively loose, it was difficult to develop the homogeneous SEI film. Accordingly, the SEI films were constantly developed during every charging process and the cycle Coulomb efficiency always declined.

**Table 5.** Cycling capability of NCM622 different ammonia content.

| NCM622 | 100th Cycling Discharge Capability (mAh $g^{-1}$) | Capacity Retention Rate (3C@100) |
|---|---|---|
| AC: 40 mL | 97.2 | 62.7% |
| AC: 50 mL | 102.6 | 63.6% |
| AC: 60 mL | 142.3 | 88.2% |
| AC: 70 mL | 150.0 | 89.8% |

Cyclic voltammogram(CV) obtained at 2.8–4.5 V (vs.Li/$Li^+$) at a scan rate of 0.1 mV $s^{-1}$ for NCM622 was exhibited in Figure 5. The redox peak on the first cyclic voltammetry curve for NCM622 from different ammonia content was not exactly symmetrical, indicating that the redox reaction of all NCM622 is partially reversible. For NCM622 (AC: 40 mL), the oxidation peak was 4.10 V, and the reduction peak is 3.45 V, indicating that $Co^{3+}/Co^{2+}$ couple was involved in the redox reaction, which is not conducive to maintaining the stability of the layered structure. In NCM622(AC: 60 mL) of CV curves, there are two oxidation peaks of 3.9 V and 4.3 V and two reduction peaks of 3.6 V and 4.1 V respectively. The ion redox sequences of the material were $Ni^{2+} \rightarrow Ni^{3+} \rightarrow Ni^{4+}$, which exactly corresponds to the two redox peaks. Because $Ni^{2+/3+}$, $Ni^{3+/4+}$ have better chemical stability, the material has good cycling performances. In CV curves of NCM622 (AC: 70 mL), Besides a pair of sharp redox peaks were observed in the range of 3.5–4.0 V corresponding to the $Ni^{2+}/Ni^{4+}$ redox couple, a strong oxidation peak of 4.0 V and a weak oxidation peak of 4.5 V were also observed. In conclusion, NCM622 (AC: 60 mL) has better cycle stability and first charge and discharge efficiency, while NCM622 (AC: 70 mL) has the highest discharge capacity.

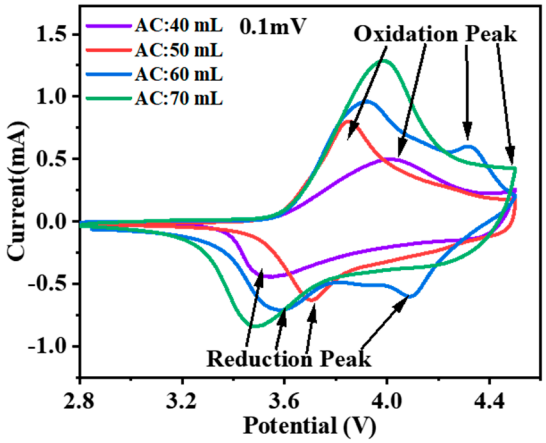


**Figure 5.** Cyclic voltammetry curve of NCM622 different ammonia content.

EIS tests were performed to explore the effect of different ammonia content on the electrochemical behavior NCM622. Equivalent series resistances were estimated from the equivalent circuit by fitting the electrochemical impedance spectrums (the inset in Figure 6a,b). The parameters of the equivalent circuit were listed in Table 6. The electrochemical kinetics of electrode materials were further evaluated by the Nyquist plots of

EIS. A small semicircle at high frequency referred to the resistance from solid electrolyte interface surface film ($R_f$), while a larger semicircle at medium frequency corresponded to the charge transfer resistance ($R_{ct}$). $R_{ct}$ was much larger than $R_f$ indicating that $R_{ct}$ was the primary factor of electrochemical reaction kinetics. As shown in Table 6, except for AC: 50 mL, the $R_f$ values decreased gradually as ammonia contents added into the reactor before co-precipitation reaction were increased. The NCM622 (AC: 50 mL) was the intermediate state from primary particles to secondary spherical particles. The specific surface area of NCM622 (AC: 50 mL) is larger than those of NCM622 (AC: 60 mL) and NCM622 (AC: 70 mL). As a consequence, the $R_f$ of NCM622 (AC: 50 mL) showed an abnormal increase. The $R_{ct}$ values of electrode materials were sharp drop with the increase of ammonia content. The $R_{ct}$ of NCM622 (AC: 70 mL) was 5 times lower than that of other materials. The 45° bias lines, corresponding to Warburg impedance ($W_o$), were slowly incline to the vertical line. The Warburg impedances gradually declined. The kinetics behavior based on concentration polarization was diminished. Consequently, the decrease of $R_{ct}$ and Warburg impedance for NCM622 (AC: 70 mL) implies its optimal kinetics behavior, demonstrating that it was necessary for enough ammonia added in the reactor before co-precipitation reaction.

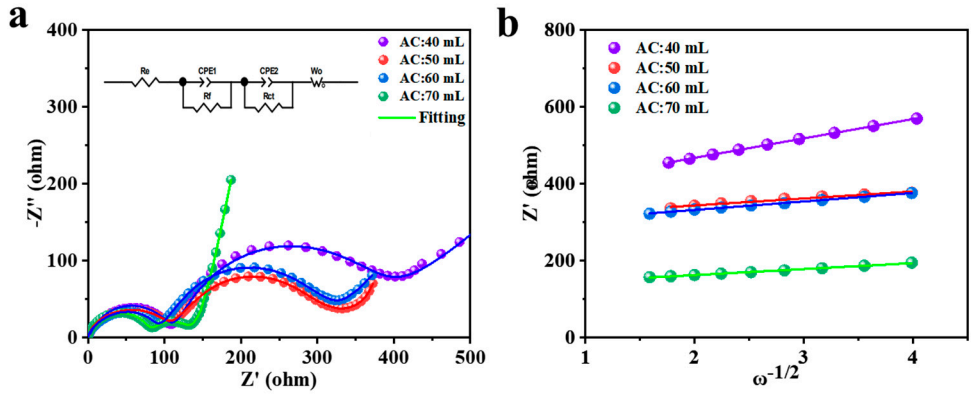


**Figure 6.** (**a**) Nyquist plots and corresponding equivalent circuit model of NCM622 different ammonia content. (**b**) the relationships between Z′ and $\omega^{-1/2}$ based on (**a**).

**Table 6.** The fitting values of $R_f$ and $R_{ct}$ and the calculated values of $D_{Li}{}^+$ of the as-prepared samples.

| Sample | $R_f$ (±Ω) | $R_{ct}$ (±Ω) | $W_o$ $R$ (±Ω) | $D_{Li}{}^+$ (cm$^2$ s$^{-1}$) |
|---|---|---|---|---|
| AC: 40 mL | 95.2 | 228.4 | 194.9 | $3.5 \times 10^{-16}$ |
| AC: 50 mL | 110.0 | 185.0 | 195.7 | $2.7 \times 10^{-15}$ |
| AC: 60 mL | 88.7 | 178.6 | 79.8 | $1.8 \times 10^{-15}$ |
| AC: 70 mL | 83.0 | 36.44 | 68.5 | $3.6 \times 10^{-15}$ |

The Lithium ions have high diffusion resistance for NCM622 (AC: 40 mL) and NCM622 (AC: 50 mL) due to their loose accumulation of secondary spheres, while the compactness and order structure for NCM622 (AC: 70 mL) is conducive to Lithium ions diffusion [32,33]. The Lithium ions diffusion resistance is closely related to Lithium ion diffusion coefficients ($D_{Li}{}^+$) calculated by Equation (1) and Warburg factor ($\sigma$) in Equation (1) calculated according to Equation (2) [34].

$$D_{Li^+} = \frac{R^2T^2}{2A^2n^4F^4C^4\sigma^2} \quad (1)$$

$$Z_{re} = R_f + R_{ct} + \sigma\omega^{-1/2} \quad (2)$$

where $R$ represents the gas constant (8.314 J mol$^{-1}$ K$^{-1}$), $T$ is thermodynamic absolute temperature (298 K). $A$ is the surface area of the electrode (1.1304 cm$^2$), $n$ is the number of the transferred electrons per molecule ($n$ = 1), $F$ represents the Faraday constant

($9.6486 \times 10^4$ C $mol^{-1}$), $C$ is the concentration of $Li^+$ in the cathode ($5.165 \times 10^2$ $mol/cm^3$), $\sigma$ is the Warburg factor which obeys the following relationship, $R_f$ is the resistance between the electrolyte and electrode, $R_{ct}$ is the charge transfer resistance and $\omega$ is the angular frequency ($\omega = 2\pi f$). Based on the Equations (1) and (2), the $D_{Li}{}^+$ of NCM622 (AC: 40 mL), NCM622 (AC: 50 mL), NCM622 (AC: 60 mL) and NCM622 (AC: 70 mL) are $3.5 \times 10^{-16}$ $cm^2/s$, $2.7 \times 10^{-15}$ $cm^2$ $s^{-1}$, $1.8 \times 10^{-15}$ $cm^2$ $s^{-1}$, $3.5 \times 10^{-15}$ $cm^2$ $s^{-1}$ and NCM622 (AC: 70 mL), respectively. The $D_{Li}{}^+$ of NCM622 (AC: 40 mL) is one order of magnitude higher than others. The larger the $D_{Li}{}^+$ is, the easier lithium ions are to be embedded into the layered structure of materials and the smaller the lithium ion diffusion resistance is. Therefore, enough ammonia added in the reactor before co-precipitation reaction is preferable to develop more suitable layered structure of NCMs for rapid Lithium intercalation behavior.

## 4. Conclusions

In summary, a facile but valid co-precipitation method was utilized to synthesize NCM622 in base solution with different ammonia content. With the increase of ammonia content before co-precipitation reaction, the primary particles of the precursor are gradually transited from irregular particles to needle and sheet morphologies, which origined from cumulation of the primary particles into the spherical secondary particles by electrostatic attraction during the dissolution and recrystallization. These compact spherical particles presented orderly and compact layered structures after lithiation and calcination, which was conducive to lithium ion intercalation into layered structures. The charge transfer resistance and Warburg impedance are also cut down. The good densely layered structure, small the Li/Ni mixing degree, the particle sizes of 5–10 μm, the uniform pore distribution, and the smallest specific surface area are revealed. It can be concluded that NCM622 (AC: 70 mL) shows the best electrochemistry performance with the initial discharge capacity of 199.8 mAh $g^{-1}$ at 0.1 C, 89.8% cycling retention rate after 100 cycles at 3 C charge-discharge circle.

**Author Contributions:** Conceptualization, X.G.; investigation, C.X.; formal analysis, L.L. and C.S.; writing—review and editing, S.G.; project administration, B.A. All authors have read and agreed to the published version of the manuscript.

**Funding:** This research was funded by the National Natural Science Foundation of China (51672118), Liao-ning Provincial Department of education project (2019LNZD01, 2017LNZD01), and Liaoning science and Technology Department Project (201602390).

**Institutional Review Board Statement:** Not applicable.

**Informed Consent Statement:** Not applicable.

**Data Availability Statement:** Not applicable.

**Conflicts of Interest:** The authors declare no conflict of interest.

## References

1. Liang, X.; Zhang, S.; Wu, Y.; Xing, J.; He, X.; Zhang, K.M.; Wang, S.; Hao, J. Air quality and health benefits from fleet electrification in China. *Nat. Sustain.* **2019**, *2*, 962–971. [CrossRef]
2. Das, R.; Wang, Y.; Putrus, G.; Kotter, R.; Marzband, M.; Herteleer, B.; Warmerdam, J. Multi-objective techno-economic-environmental optimisation of electric vehicle for energy services. *Appl. Energy* **2020**, *257*, 113965. [CrossRef]
3. Zhang, X.; Zou, L.; Cui, Z.; Jia, H.; Engelhard, M.H.; Matthews, B.E.; Cao, X.; Xie, Q.; Wang, C.; Manthiram, A.; et al. Stabilizing ultrahigh-nickel layered oxide cathodes for high-voltage lithium metal batteries. *Mater. Today* **2021**, *44*, 15–24. [CrossRef]
4. Yin, S.; Deng, W.; Chen, J.; Gao, X.; Zou, G.; Hou, H.; Ji, X. Fundamental and solutions of microcrack in Ni-rich layered oxide cathode materials of lithium-ion batteries. *Nano Energy* **2021**, *83*, 105854. [CrossRef]
5. Somo, T.; Mabokela, T.; Teffu, D.; Sekgobela, T.; Ramogayana, B.; Hato, M.; Modibane, K. A Comparative Review of Metal Oxide Surface Coatings on Three Families of Cathode Materials for Lithium Ion Batteries. *Coatings* **2021**, *11*, 744. [CrossRef]
6. Meng, J.; Chu, F.; Hu, J.; Li, C. Liquid Polydimethylsiloxane Grafting to Enable Dendrite-Free Li Plating for Highly Reversible Li-Metal Batteries. *Adv. Funct. Mater.* **2019**, *29*, 1902220. [CrossRef]
7. Lu, J.; Xu, C. An Effective Way to Stabilize Ni-Rich Layered Cathodes. *Chem* **2020**, *6*, 3165–3167. [CrossRef]

8. Mäntymäki, M.; Ritala, M.; Leskelä, M. Metal Fluorides as Lithium-Ion Battery Materials: An Atomic Layer Deposition Perspective. *Coatings* **2018**, *8*, 277. [CrossRef]
9. Huang, Y.; Dong, Y.; Li, S.; Lee, J.; Wang, C.; Zhu, Z.; Xue, W.; Li, Y.; Li, J. Lithium Manganese Spinel Cathodes for Lithium-Ion Batteries. *Adv. Energy Mater.* **2021**, *11*, 2000997. [CrossRef]
10. Sawamura, M.; Kobayakawa, S.; Kikkawa, J.; Sharma, N.; Goonetilleke, D.; Rawal, A.; Shimada, N.; Yamamoto, K.; Yamamoto, R.; Zhou, Y.; et al. Nanostructured LiMnO2 with Li3PO4 Integrated at the Atomic Scale for High-Energy Electrode Materials with Reversible Anionic Redox. *ACS Cent. Sci.* **2020**, *6*, 2326–2338. [CrossRef] [PubMed]
11. Marincaş, A.-H.; Ilea, P. Enhancing Lithium Manganese Oxide Electrochemical Behavior by Doping and Surface Modifications. *Coatings* **2021**, *11*, 456. [CrossRef]
12. Huang, Y.; Zhu, Y.; Fu, H.; Ou, M.; Hu, C.; Yu, S.; Hu, Z.; Chen, C.; Jiang, G.; Gu, H.; et al. Mg-Pillared LiCoO2: Towards Stable Cycling at 4.6 V. *Angew. Chem.* **2021**, *133*, 4732–4738. [CrossRef]
13. Yang, X.-G.; Liu, T.; Wang, C.-Y. Thermally modulated lithium iron phosphate batteries for mass-market electric vehicles. *Nat. Energy* **2021**, *6*, 176–185. [CrossRef]
14. Guo, J.; Wu, F. Preparation of Nano-spherical Iron Phosphate by Hydrothermal Method and Its Application as the Precursor of Lithium Iron Phosphate. *J. Electrochem. Energy Convers. Storage* **2020**, *18*, 1–9. [CrossRef]
15. Kong, F.; Liang, C.; Wang, L.; Zheng, Y.; Perananthan, S.; Longo, R.C.; Ferraris, J.P.; Kim, M.; Cho, K. Kinetic Stability of Bulk LiNiO2 and Surface Degradation by Oxygen Evolution in LiNiO2 -Based Cathode Materials. *Adv. Energy Mater.* **2019**, *9*, 1802586. [CrossRef]
16. Yoon, C.S.; Kim, U.-H.; Park, G.-T.; Kim, S.J.; Kim, K.-H.; Kim, J.; Sun, Y.-K. Self-Passivation of a LiNiO2 Cathode for a Lithium-Ion Battery through Zr Doping. *ACS Energy Lett.* **2018**, *3*, 1634–1639. [CrossRef]
17. Bi, Y.; Tao, J.; Wu, Y.; Li, L.; Xu, Y.; Hu, E.; Wu, B.; Hu, J.; Wang, C.; Zhang, J.-G.; et al. Reversible planar gliding and microcracking in a single-crystalline Ni-rich cathode. *Science* **2020**, *370*, 1313–1317. [CrossRef] [PubMed]
18. Kim, U.-H.; Park, G.-T.; Conlin, P.; Ashburn, N.; Cho, K.; Yu, Y.-S.; Shapiro, D.A.; Maglia, F.; Kim, S.-J.; Lamp, P.; et al. Cation ordered Ni-rich layered cathode for ultra-long battery life. *Energy Environ. Sci.* **2021**, *14*, 1573–1583. [CrossRef]
19. Han, Y.; Jung, S.H.; Kwak, H.; Jun, S.; Kwak, H.H.; Lee, J.H.; Hong, S.; Jung, Y.S. Single- or Poly-Crystalline Ni-Rich Layered Cathode, Sulfide or Halide Solid Electrolyte: Which Will be the Winners for All-Solid-State Batteries? *Adv. Energy Mater.* **2021**, *11*, 2100126. [CrossRef]
20. Shi, Y.; Zhang, M.; Fang, C.; Meng, Y.S. Urea-based hydrothermal synthesis of LiNi0.5Co0.2Mn0.3O2 cathode material for Li-ion battery. *J. Power Sources* **2018**, *394*, 114–121. [CrossRef]
21. Ma, C. Hydrothermal Synthesis and Electrochemical Performance of Micro-spherical LiNi1/3Co1/3Mn1/3O2 Cathode Material. *Int. J. Electrochem. Sci.* **2020**, *15*, 9392–9401. [CrossRef]
22. Purwanto, A.; Yudha, C.S.; Muhammad, K.I.; Algifari, B.G.; Widiyandari, H.; Sutopo, W. Synthesis of LiNi0.8Co0.15Al0.05O2 cathode material via flame-assisted spray pyrolysis method. *Adv. Powder Technol.* **2020**, *31*, 1674–1681. [CrossRef]
23. Gui, S.; Zhang, Q.; Zhuo, H.; Liu, J. Enhancing the electrochemical performance of LiNi0.8Co0.15Al0.05O2 by a facile doping method: Spray-drying doping with liquid polyacrylonitrile. *J. Power Sources* **2019**, *409*, 102–111. [CrossRef]
24. Lu, S.-J.; Liu, Y.; He, Z.-J.; Li, Y.-J.; Zheng, J.-C.; Mao, J.; Dai, K.-H. Synthesis and properties of single-crystal Ni-rich cathode materials in Li-ion batteries. *Trans. Nonferrous Met. Soc. China* **2021**, *31*, 1074–1086. [CrossRef]
25. Shen, Y.; Wu, Y.; Xue, H.; Wang, S.; Yin, D.; Wang, L.; Cheng, Y. Insight into the Coprecipitation-Controlled Crystallization Reaction for Preparing Lithium-Layered Oxide Cathodes. *ACS Appl. Mater. Interfaces* **2021**, *13*, 717–726. [CrossRef]
26. Voorhees, P.W. The theory of Ostwald ripening. *J. Stat. Phys.* **1985**, *38*, 231–252. [CrossRef]
27. Gao, Y.; Wang, Z.; Lu, G. Atomistic understanding of structural evolution, ion transport and oxygen stability in layered $NaFeO_2$. *J. Mater. Chem. A* **2019**, *7*, 2619–2625. [CrossRef]
28. Li, D.; Sasaki, Y.; Kobayakawa, K.; Sato, Y. Morphological, structural, and electrochemical characteristics of $LiNi_{0.5}Mn_{0.4}M_{0.1}O_2$ (M=Li, Mg, Co, Al). *J. Power Sources* **2006**, *157*, 488–493. [CrossRef]
29. Li, D.-C.; Muta, T.; Zhang, L.-Q.; Yoshio, M.; Noguchi, H. Effect of synthesis method on the electrochemical performance of $LiNi_{1/3}Mn_{1/3}Co_{1/3}O_2$. *J. Power Sources* **2004**, *132*, 150–155. [CrossRef]
30. Xiao, P.; Lv, T.; Chen, X.; Chang, C. LiNi0.8Co0.15Al0.05O2: Enhanced Electrochemical Performance From Reduced Cationic Disordering in Li Slab. *Sci. Rep.* **2017**, *7*, 1–8. [CrossRef]
31. Geng, X.; Li, L.; Li, F. Carbon nanotubes/activated carbon hybrid with ultrahigh surface area for electrochemical capacitors. *Electrochim. Acta* **2015**, *168*, 25–31. [CrossRef]
32. Kim, T.; Ono, L.K.; Fleck, N.; Raga, S.R.; Qi, Y. Transition metal speciation as a degradation mechanism with the formation of a solid-electrolyte interphase (SEI) in Ni-rich transition metal oxide cathodes. *J. Mater. Chem. A* **2018**, *6*, 14449–14463. [CrossRef]
33. Ahmad, H.M.N.; Ghosh, S.; Dutta, G.; Maddaus, A.G.; Tsavalas, J.G.; Hollen, S.; Song, E. Effects of Impurities on the Electrochemical Characterization of Liquid-Phase Exfoliated Niobium Diselenide Nanosheets. *J. Phys. Chem. C* **2019**, *123*, 8671–8680. [CrossRef]
34. Zheng, F.; Ou, X.; Pan, Q.; Xiong, X.; Yang, C.; Fu, Z.; Liu, M. Nanoscale gadolinium doped ceria (GDC) surface modification of Li-rich layered oxide as a high performance cathode material for lithium ion batteries. *Chem. Eng. J.* **2018**, *334*, 497–507. [CrossRef]